



# Cross-hole electromagnetic and seismic modeling for CO<sub>2</sub> detection and monitoring in a saline aquifer

José M. Carcione<sup>a,\*</sup>, Davide Gei<sup>a</sup>, Stefano Picotti<sup>a</sup>, Alberto Michelini<sup>b</sup>

<sup>a</sup> Istituto Nazionale di Oceanografia e di Geofisica Sperimentale (OGS), Borgo Grotta Gigante 42c, 34010 Sgonico, Trieste, Italy

<sup>b</sup> Istituto Nazionale di Geofisica e Vulcanologia (INGV), Via di Vigna Murata, 605, 00143 Roma, Italy

## ARTICLE INFO

### Article history:

Received 23 July 2011

Accepted 15 March 2012

Available online 30 March 2012

### Keywords:

electromagnetic modeling

seismic modeling

CO<sub>2</sub> detection

## ABSTRACT

The injection of CO<sub>2</sub> in saline aquifers and depleted hydrocarbon wells is one solution to avoid the emission of that greenhouse gas to the atmosphere. Carbon taxes can be avoided if geological sequestration can efficiently be performed from technical and economic perspectives. For this purpose, we present a combined rock-physics methodology of electromagnetic (EM) and seismic wave propagation for the detection and monitoring of CO<sub>2</sub> in crosswell experiments.

First, we obtain the electrical conductivity and seismic velocities as a function of saturation, porosity, permeability and clay content, based on the CRIM and White models, respectively. Then, we obtain a conductivity–velocity relation. This type of relations is useful when some rock properties can be more easily measured than other properties. Finally, we compute crosswell EM and seismic profiles using direct modeling techniques. P- and S-wave attenuation is included in the seismic simulation by means of White's mesoscopic theory. The modeling methodology is useful to perform sensitivity analyses and it is the basis for performing traveltime EM and seismic tomography and obtain reliable estimations of the saturation of carbon dioxide. In both cases, it is essential to correctly pick the first arrivals, particularly in the EM case where diffusion wavelength is large compared to the source–receiver distance.

The methodology is applied to CO<sub>2</sub> injection in a sandstone aquifer with shale intrusions, embedded in a shale formation. The EM traveltimes are smaller after the injection due to the higher resistivity caused by the presence of carbon dioxide, while the effect is opposite in the seismic case, where water replaced by gas decreases the seismic velocity.

© 2012 Elsevier B.V. All rights reserved.

## 1. Introduction

Geological sequestration is an immediate option to solve in part the problem of carbon-dioxide emission to the atmosphere. Feasible possibilities are injection into hydrocarbon reservoirs and saline aquifers (Alavian and Whitson, 2011; Arts et al., 2004; Carcione et al., 2006). It is essential in CO<sub>2</sub> sequestration to monitor the injected plumes as they diffuse into the reservoir, and any leakage has to be carefully monitored. The loss of integrity of the cap rock above the reservoir and the potential for leakage along bedding planes, faults and fractures should be detected. Seismic and electromagnetic (EM) methods can be used for non-invasive determination of subsurface physical and chemical properties (Giese et al., 2009). Seismic measurements provide P- and S-wave velocities and attenuations, while electromagnetic data at

low frequencies provide electrical conductivity, which can be related to fluid saturation. The combined use of these methods can give more reliable results if the interpretation is based on suitable cross-property relations between seismic velocity and conductivity (Carcione et al., 2007). In particular, the electrical conductivity of reservoir rocks is highly sensitive to changes in water and CO<sub>2</sub> saturation and on a lesser degree the P-wave velocity, while the S-wave velocity remains nearly constant.

A few authors have used EM methods to monitor CO<sub>2</sub> in the underground. Norman et al. (2008) built a resistivity model from seismic data and Archie's law. The time-lapse responses for the 2001 and 2006 plumes at Sleipner versus the case without CO<sub>2</sub> indicate peak anomalies of 25% and 50% at 3 km offset, respectively. Bourgeois et al. (2009) performed a feasibility study of monitoring a supercritical CO<sub>2</sub> injection in a deep saline aquifer by means of EM methods, where the source is a deep metallic casing.

Hoversten et al. (2004) performed crosswell seismic and EM imaging to produce a velocity tomogram and a conductivity section to derive porosity and water saturation. They found a

\* Corresponding author.

E-mail addresses: [jcarcione@inogs.it](mailto:jcarcione@inogs.it) (J.M. Carcione), [alberto.michelini@ingv.it](mailto:alberto.michelini@ingv.it) (A. Michelini).

poor petrophysical relationship between velocity and porosity, clay content, and water saturation, but strong petrophysical relations between electrical conductivity and these parameters. In [Hoversten et al. \(2006\)](#), the authors link reservoir parameters to geophysical parameters through a rock-properties model. The adopted model is the Hertz–Mindlin contact theory for the dry frame and modified Hashin–Shtrikman lower bounds to calculate the effective moduli. On the other hand, Archie's law is used to model electrical resistivity as a function of porosity and water saturation. [Lei and Xue \(2009\)](#) performed laboratory measurements at ultrasonic frequencies during the injection of CO<sub>2</sub> into a water-saturated sandstone sample. CO<sub>2</sub> migration and water displacement were mapped using tomographic images of velocity and quality factor. On average, the P-wave velocity decreased by 7.5%, 12%, and 14.5% and the inverse quality factor increased by factors of 3.3, 2.7, and 3.7 as a result of the replacement of water with CO<sub>2</sub> during the injection of gaseous, liquid, and supercritical CO<sub>2</sub>, respectively. Both the velocity and attenuation data were in good agreement with White's model used in the present work.

Electrical resistivity tomography (ERT) in crosswell configurations is another technique being employed for detecting CO<sub>2</sub>. [Christensen et al. \(2006\)](#) have shown the potential of ERT to detect the resistivity changes caused by CO<sub>2</sub> injection and migration in geological reservoirs. Recently, [Hagrey \(2010\)](#) performed an ERT crosswell numerical study and showed that the method can discriminate the various components of a CO<sub>2</sub> storage in conductive saline reservoirs, namely, the plume, the host reservoir, and the cap rock.

In this work, we deal with transient fields that can be processed to obtain the electrical conductivity with cross-hole experiments (e.g., [Wilt et al., 1995](#)). We use the White/CRIM relation between seismic velocity and electrical conductivity, which has been successfully tested with well-log data of the North Sea ([Carcione et al., 2007](#)). This relation provides a reasonable fit to the data, indicating that it is possible to predict an electrical property from an elastic property and vice versa. Then, we perform a sensitivity analysis by computing the EM field and synthetic seismograms corresponding to a geological model of CO<sub>2</sub> partial saturation, based on a cross-hole source–receiver configuration. Finally, we obtain traveltimes picks (first arrival versus receiver locations) which are the basis for EM and seismic tomography.

## 2. The cross-property relation between conductivity and seismic velocity

The key property to relate the electrical conductivity to the P- and S-wave velocities is the porosity. Assume that the conductivity and velocity have the form  $\sigma = f(\phi)$  and  $v = g(\phi)$ , where  $\phi$  is the porosity. Then, the relation is given by  $\sigma = f[g^{-1}(v)]$ . This simple 1D concept is quite general and can be applied to higher spatial dimensions and the case of anisotropy (e.g., [Carcione et al., 2007](#); [Kachanov et al., 2001](#)).

### 2.1. Electromagnetic properties. CRIM model

The complex refractive index method (CRIM) for a shaly sandstone with negligible permittivity and partially saturated with gas, can be expressed as

$$\sigma = [(1-\phi)(1-C)\sigma_q^\gamma + (1-\phi)C\sigma_c^\gamma + \phi(1-S_g)\sigma_b^\gamma + \phi S_g\sigma_g^\gamma]^{1/\gamma}, \quad \gamma = 1/2 \quad (1)$$

([Carcione, 2007](#); [Carcione et al., 2007](#); [Schön, 1996](#)), where  $\sigma_q$ ,  $\sigma_c$ ,  $\sigma_b$  and  $\sigma_g$  are the sand-grain (quartz), clay, brine and gas conductivities,  $C$  is the clay content, and  $S_g$  is the gas saturation.

If  $\gamma$  is a free parameter, the equation is termed Lichtnecker–Rother formula. It is based on the ray approximation. The travel time in each medium is inversely proportional to the electromagnetic velocity, which in turn is inversely proportional to the square root of the complex dielectric constant. At low frequencies, displacement currents can be neglected and Eq. (1) is obtained. Generally  $\sigma_q = \sigma_g = 0$  and Eq. (1) becomes

$$\sigma = [(1-\phi)C\sigma_c^\gamma + \phi(1-S_g)\sigma_b^\gamma]^{1/\gamma}, \quad \gamma = 1/2. \quad (2)$$

For zero clay content, Eq. (2) is exactly Archie's law used in [Hoversten et al. \(2006\)](#).

### 2.2. Elastic properties. White model

The seismic velocities and quality factors are determined from a mesoscopic rock-physics theory ([White, 1975](#)), which provides realistic values as a function of porosity, gas saturation, clay content, fluid viscosity and permeability ([Appendix A](#)). It is assumed that the medium has patches of CO<sub>2</sub> in a brine saturated background, where brine has absorbed the maximum amount of CO<sub>2</sub>. White's model (see [Carcione et al., 2003](#)) describes wave velocity and attenuation as a function of frequency. We introduce shear dissipation as indicated in [Appendix A](#), and for a given reference frequency,  $f_0$ , which is the dominant source frequency, we obtain the P- and S-wave phase velocities. The model depends on the patch size  $r_0$ . White assumed spherical gas pockets much larger than the grains but much smaller than the wavelength. He developed the theory for a gas-filled sphere of porous medium of radius  $r_0$  located inside a water-filled cube of porous medium. For simplicity in the calculations, White considered an outer sphere of radius  $r_1$  ( $r_1 > r_0$ ), instead of a cube, where  $S_g = r_0^3/r_1^3$ . More details can be found in [White \(1975\)](#), [Carcione et al. \(2003\)](#) and [Carcione \(2007\)](#).

For homogeneous waves in isotropic media, the phase velocity and attenuation factors are given by

$$v_p = \left[ \operatorname{Re}\left(\frac{1}{v}\right) \right]^{-1} \quad \text{and} \quad \alpha = -\omega \operatorname{Im}\left(\frac{1}{v}\right), \quad (3)$$

respectively, where  $v$  denotes the complex velocity of the wave mode, and  $\omega$  is the angular frequency  $\omega = 2\pi f$ . The corresponding quality factor is

$$Q = \frac{\operatorname{Re}(v^2)}{\operatorname{Im}(v^2)}, \quad (4)$$

and the quality factor associated with White bulk modulus  $K$  is

$$\frac{\operatorname{Re}(K)}{\operatorname{Im}(K)}. \quad (5)$$

The P- and S-wave complex velocities of the partially saturated porous medium are

$$v_p = \sqrt{\frac{1}{\rho} \left( K + \frac{4}{3}\mu \right)} \quad \text{and} \quad v_s = \sqrt{\frac{\mu}{\rho}}, \quad (6)$$

respectively, where  $\mu$  is the shear complex modulus of the matrix as given in [Appendix A](#) (Eq. (21)). The density of the medium is

$$\rho = (1-\phi)[(1-C)\rho_q + C\rho_c] + \phi\rho_f, \quad (7)$$

where  $\rho_q$  and  $\rho_c$  are the sand-grain (quartz) and clay densities, respectively, and

$$\rho_f = S_g\rho_g + (1-S_g)\rho_b \quad (8)$$

is the density of the gas–liquid mixture, where  $\rho_g$  and  $\rho_b$  are the gas and brine densities, respectively.

The presence of clay modifies the effective bulk and shear moduli of the grains,  $K_s$  and  $\mu_s$ . That is, the grains are formed by a mixture of quartz and clay. We assume that this moduli are equal

to the arithmetic average of the upper and lower Hashin–Shtrikman bounds (Hashin and Shtrikman, 1963; Mavko et al., 1998).

The bulk modulus of the matrix is obtained by using Krief model. A suitable expression is

$$K_m = K_s(1-\phi)^{\mathcal{A}/(1-\phi)}, \quad (9)$$

where  $\mathcal{A}$  is a dimensionless parameter which depends on the pore shape and Poisson ratio of the matrix. This parameter is a pore compliance coefficient, and takes a value of about 2 for spherical pores, increasing as the pores become more crack-like (David and Zimmerman, 2011; Le Ravalec and Gueguen, 1996). We assume the dry-rock shear modulus

$$\mu_m = \frac{\mu_s}{K_s} K_m. \quad (10)$$

This relation implies that the Poisson ratio of the dry porous rock is equal to the Poisson ratio of the mineral forming the rock frame. This is generally not the case (David and Zimmerman, 2011; Le Ravalec and Gueguen, 1996), but that simplification is used in the absence of data to calibrate the model. An alternative model, based on the DEM theory (Li and Zhang, 2011), can be used if one has information about the dominant aspect ratio of the pores. In a real situation, one could evaluate the dry-rock moduli from the wet-rock moduli obtained from sonic-log data (by using the inverse Gassmann's equations), or obtain those moduli from cores by measuring the P- and S-wave velocities in the laboratory.

As mentioned above, to relate the velocities to the conductivities, we replace  $\phi = \phi(\sigma)$  [taken from Eq. (1)] into Eq. (6), where

$$\phi(\sigma) = \frac{\sigma^\gamma - (1-C)\sigma_b^\gamma - C\sigma_g^\gamma}{(1-S_g)\sigma_b^\gamma + S_g\sigma_g^\gamma - (1-C)\sigma_d^\gamma - C\sigma_c^\gamma} \quad (\gamma = 1/2 \text{ CRIM}). \quad (11)$$

### 3. Modeling methods

#### 3.1. Electromagnetic modeling

The modeling method to compute diffusion fields is that of Carcione (2006, 2007, 2010), who proposed a spectral algorithm to solve the electromagnetic diffusion equation. Let us assume that the material properties and the source are invariant in the  $y$ -direction. Then, the propagation can be described in the  $(x,z)$ -plane, and  $E_x$ ,  $E_z$  and  $H_y$  are decoupled from  $E_y$ ,  $H_x$  and  $H_z$ , corresponding to the so-called TM (transverse magnetic) and TE (transverse electric) equations, where  $E$  and  $H$  denote electric and magnetic fields, respectively. The TM equation is

$$\mu_0 \dot{H}_y = (\sigma^{-1} H_{y,x})_x + (\sigma^{-1} H_{y,z})_z - \mu_0 \dot{M}_y + (J_{x,z} - J_{z,x}), \quad (12)$$

where  $\mu_0$  is the magnetic permeability of vacuum and  $M_y$  and  $J$  are magnetic and electric sources, respectively. A dot above a variable denotes time differentiation, and the subindices,  $x$  and  $z$  indicate spatial derivatives with respect to the Cartesian coordinates. Electric-field components can be computed by using Maxwell's equations,

$$\begin{pmatrix} E_x \\ E_z \end{pmatrix} = \frac{1}{\sigma} \begin{pmatrix} -\partial_z H_y \\ \partial_x H_y \end{pmatrix}. \quad (13)$$

The algorithm uses an explicit scheme based on a Chebyshev expansion of the evolution operator, and the spatial derivatives are computed with a pseudospectral method, which allows the use of coarser grids compared to finite-difference methods (see Appendix B). The modeling allows general material variability and provides snapshots and time histories of the electric and magnetic fields.

#### 3.2. Seismic modeling

The synthetic seismograms are computed with a modeling code based on an isotropic and viscoelastic stress–strain relation. The equations are given in Section 3.9 of Carcione (2007) and were first introduced by Carcione et al. (1988) (see Appendix C). The algorithm is based on the Fourier pseudospectral method for computing the spatial derivatives and a 4th-order Runge–Kutta technique for calculating the wavefield recursively in time.

The wave equation and propagation properties are given in Appendix C, where it is shown how to obtain the viscoelastic parameters. Shear loss is modeled as indicated in the appendices, where a viscoelastic extension of White's theory has been performed.

### 4. Examples and simulations

The properties of the shaly sandstone are given in Table 1. Fig. 1 shows the conductivity  $\sigma$  as a function of the gas saturation  $S_g$  and clay content  $C$ . As expected, decreasing conductivity is associated with increasing gas saturation, as well as decreasing clay content.

The P-wave and S-wave velocities at  $f_0=200$  Hz are displayed in Fig. 2 as a function of gas saturation and different values of clay content.  $\mathcal{A}=3$  is used in Eq. (9). The velocities have a minimum value depending on the clay content. The velocity increase with clay at a fixed low saturation is due to the fact that a small amount of clay induces a substantial decrease in permeability in the range  $C=[5,10]\%$ , and this generates a rock stiffening, i.e., White's bulk modulus increases. This poroelastic effect mainly affects factor  $W$  [see Eq. (16)]. However, the dominant trend is a velocity decrease due to the substitution of brine by gas, while beyond that range fluid density effects are more important and the velocities increase. The density effects affect the whole range

**Table 1**

Elastic and electromagnetic properties.

Medium	$K$ (GPa)	$\mu$ (GPa)	$\rho$ (g/cm <sup>3</sup> )	$R$ ( $\mu$ m)	$\eta$ (Pa s)	$\sigma$ (S/m)
Clay	25	20	2.65	1	–	0.2
Sand grains	39	40	2.65	50	–	0.01
Brine	2.25	0	1.03	–	0.0012	12
CO <sub>2</sub>	0.025	0	0.5	–	0.00002	0

$\phi = 25\%$ ,  $r_1 = 10$  cm.

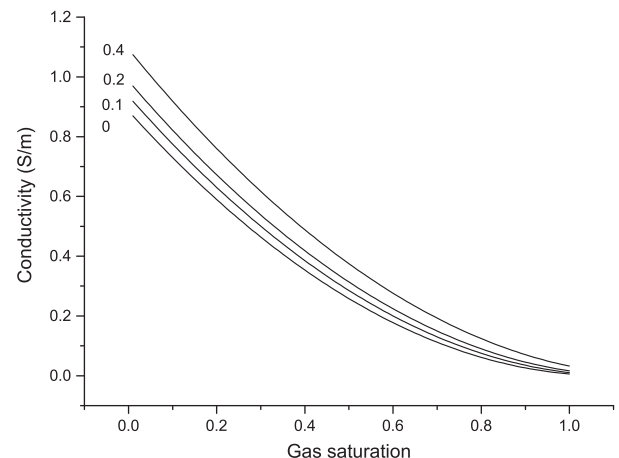


**Fig. 1.** Rock conductivity as a function of gas saturation. The numbers indicate the clay content.

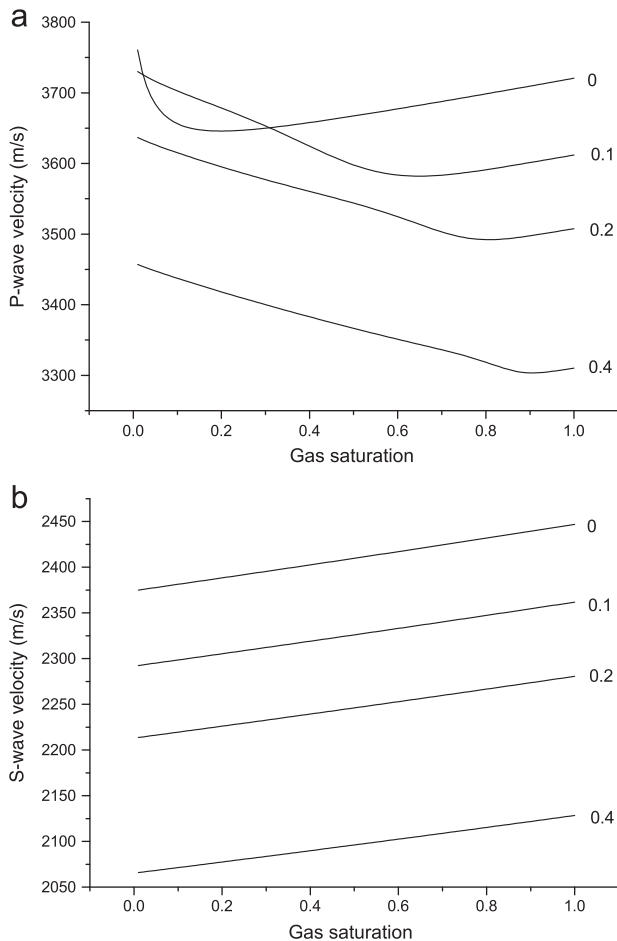


**Fig. 2.** P-wave (a) and S-wave (b) velocities as a function of gas saturation at 200 Hz. The numbers indicate the clay content.

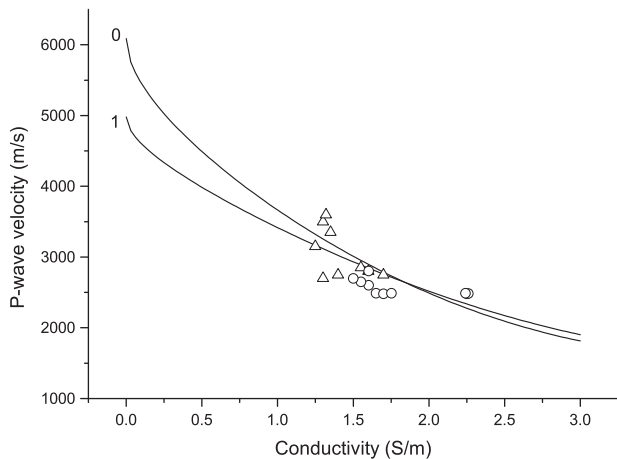


**Fig. 3.** P-wave velocity as a function of the conductivity, where the brine saturation is 100%. The numbers indicate the clay content, and the triangles and circles correspond to the sandy and shaly sections of the well.

of saturations in the S-wave velocity. Generally, when the clay content increases the velocities decrease as expected.

Next, we analyze the cross-property relation between velocity and conductivity. We consider well-log data of the Gullfaks field in the North Sea. The well is vertical and consists of sand and shale filled with brine. The velocity–conductivity relation is shown in Fig. 3, where the numbers correspond to the clay content. The curves show a good agreement with the data. Fig. 4

shows the cross-property relation between the wave velocities and the conductivity for  $S_g=0.1$  and  $S_g=0.4$ . Higher velocity is associated with lower conductivity, while at the same value of the velocity, the conductivity is lower for higher gas saturation. At high saturations and conductivities the relation does not yield realistic values of the velocities, because the curves are generated by taking the conductivity as the independent variable, and beyond a given threshold the conductivity values are not compatible with high gas saturation.

Fig. 5 displays the P-wave phase velocity (a) and the dissipation factor (b) as a function of gas saturation and three values of the clay content. As can be seen, the quality factor has a maximum at 8% gas saturation in the absence of clay content and the peak moves to higher saturations for increasing clay content.

The conductivity can be related to the hydraulic permeability through the porosity. Fig. 6 shows the permeability as a function of conductivity for a clean sandstone (0) and pure shale (1). As expected, the conductivity increases with increasing permeability, since the electrolytic conduction of ions increases with permeability.

We obtain in Appendix D the electromagnetic Green's function and indicate how to obtain the traveltimes of the first arrival. This is needed to perform, for instance, traveltimes tomography (Brauchler et al., 2003; Lee and Uchida, 2005; Lee et al., 2002; Michelini, 1995). The Green function for  $\sigma=0.2$  S/m is given in Fig. 7, where the signals at two receivers are shown. Note that the abscissa is the logarithm of time. This means that at earlier times

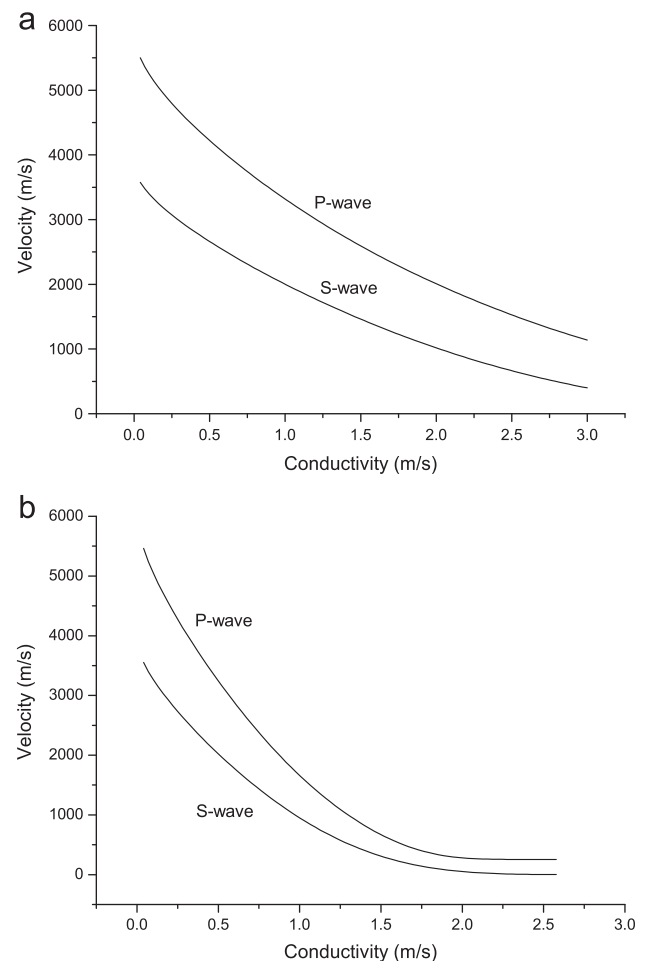


**Fig. 4.** P- and S-wave velocities as a function of the conductivity at a frequency of 200 Hz. The clay content is  $C=0.2$  and the gas saturation is  $S_g=0.1$  (a) and 0.4 (b).

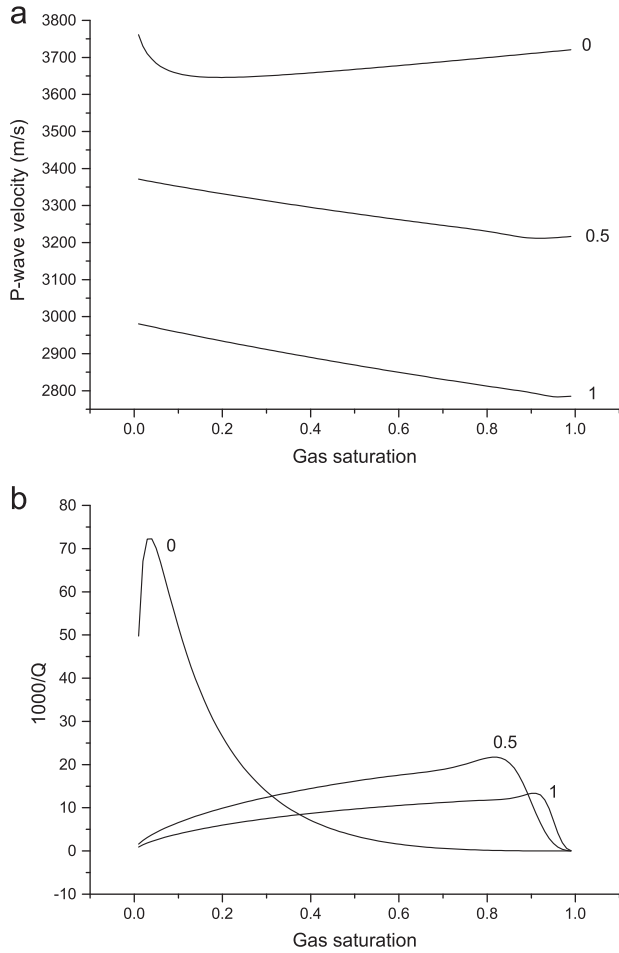


**Fig. 5.** P-wave velocity (a) and dissipation factor (b) as a function of the saturation for 0%, 50% and 100% clay content. The frequency is 200 Hz.

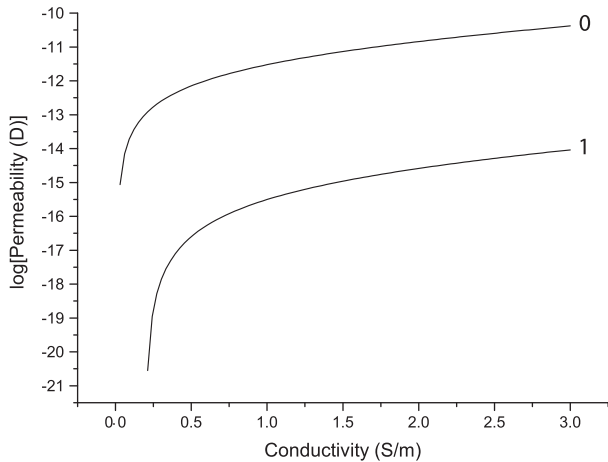


**Fig. 6.** Permeability as a function of conductivity for  $C=0$  (clean sandstone) and  $C=1$  (shale) ( $-12$  correspond to  $1D$ ).

the signal is very steep and then decays smoothly. The peak times,  $t_p$ , are  $6.28 \mu s$  and  $628 \mu s$ , respectively. Diffusion fields resemble waves in a log time scale. A test of the modeling algorithm is displayed in Fig. 8, where the dots correspond to the numerical solution. The medium is homogeneous with  $\sigma=0.2 S/m$  and  $\mu=\mu_0=4\pi \times 10^{-7} H/m$  (magnetic permeability of vacuum). The number of grid points is  $n_x=n_z=315$  and the grid spacing  $dx=dz=2.5 m$ . The computations use  $b=1.2 \times 10^7/s$  and  $M=14\,000$

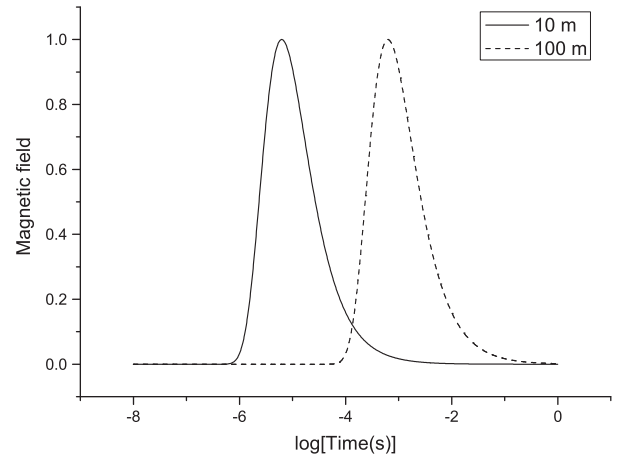


**Fig. 7.** Electromagnetic Green's function as a function of time at two receivers. The fields are normalized and the signal at 100 m has an amplitude 100 times weaker than the signal at 10 m.

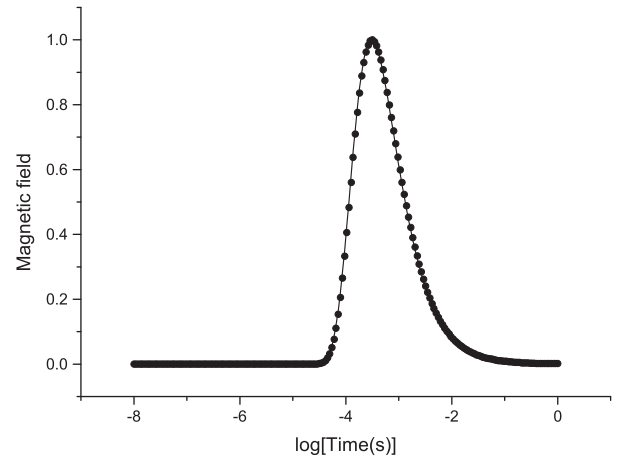


**Fig. 8.** Comparison between numerical and analytical solutions (normalized) at  $(x,z)=(50,50) m$  ( $r \approx 70 m$ ) from the source location (center of the mesh). The solid line corresponds to the analytical solution, obtained from Eq. (41).

at 1 s propagation time (these are maximum values) (see Appendix B). The same solution can be obtained with  $b=780\,000/s$  and  $M=3500$ , i.e., less computer time, using  $dx=dz=10 m$ , at the expense of a coarser grid. The numerical solver needs to be more accurate than in the seismic case, since the peak is located at 0.3 ms, while the signal still decays with a finite amplitude at 1 s propagation time, i.e., the solver has to capture the solution till 3000 times the onset time.

Let us consider a realistic example, with a regular numerical mesh with grid spacing  $dx=dz=2.5 m$ . The model is a sandstone aquifer with shale intrusions, embedded in a shale formation. The properties at each grid point in the sandstone layer are obtained as follows:

- (i) set the porosity  $\phi$ , clay content  $C$  and saturation  $S_g$ ;
- (ii) use Eq. (1) to obtain the conductivity;
- (iv) obtain the seismic velocities at  $f_0$  using Eq. (3);
- (v) obtain the quality factor  $Q_0$  from Eq. (20) and set  $Q_0^{(1)}=Q_0$  and calculate  $Q_0^{(2)}$  from Eq. (19). The relaxation times are obtained using Eq. (32);
- (vi) compute the density from Eq. (7).

It is assumed that  $\mathcal{A}=3$  in Eq. (9) and  $2\pi\tau_0 f_0=1$ , where  $f_0=150 Hz$ . We consider the model shown in Fig. 9, which shows the porosity (a), clay content (b), permeability (c) and gas



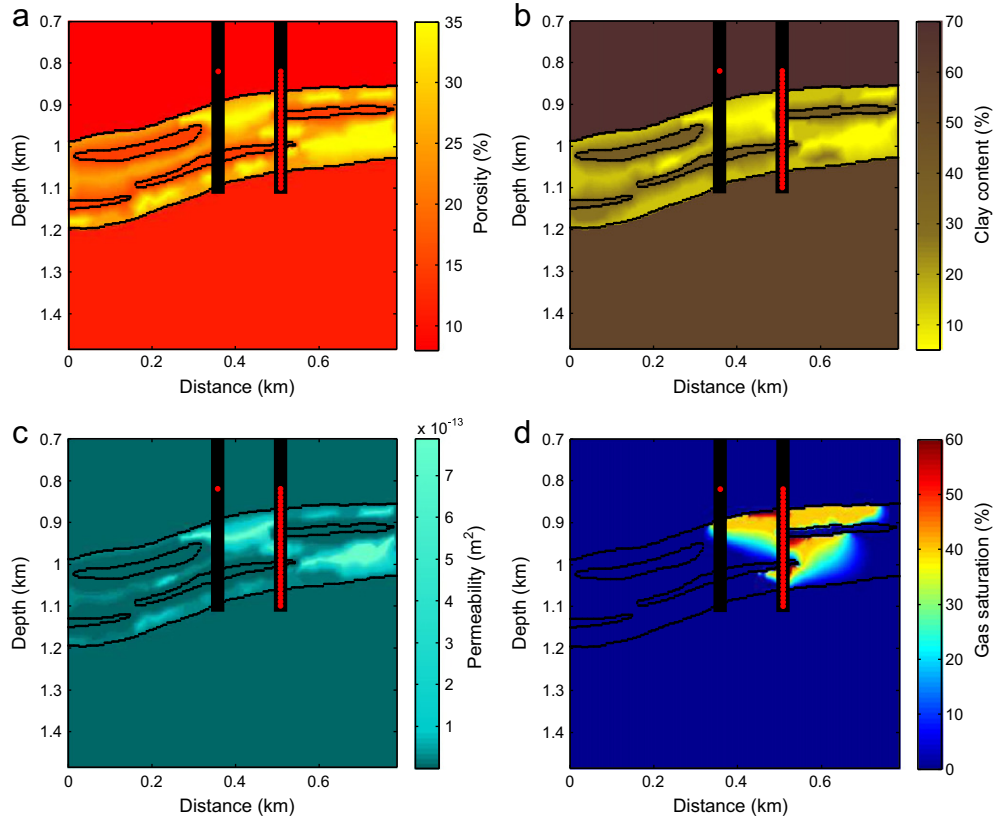


**Fig. 9.** Porosity (a), clay content (b), permeability (c) and CO<sub>2</sub> saturation after the injection (d). The locations of the source (left) and receiver (right) wells are indicated.

saturation after the injection (d). Before the injection, the layer is fully saturated with water ( $S_g=0$ ). The conductivity before and after the injection is shown in Fig. 10. On the other hand, Fig. 11 displays the seismic properties of the same model, before and after the injection.

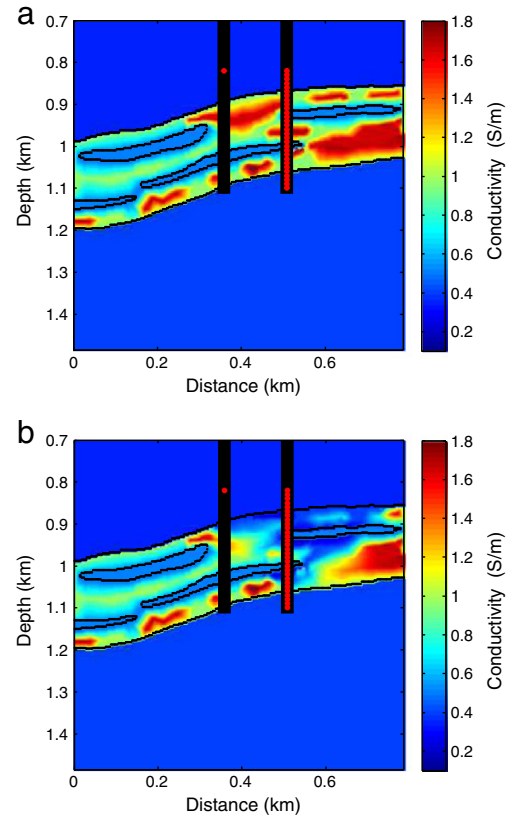
Both, the EM and seismic meshes have  $315 \times 315$  points with square cells of  $dx=dz=2.5$  m size. The source time history is

$$h(t) = \left(u - \frac{1}{2}\right) \exp(-u), \quad u = \left[\frac{\pi(t-t_s)}{T}\right]^2, \quad (14)$$

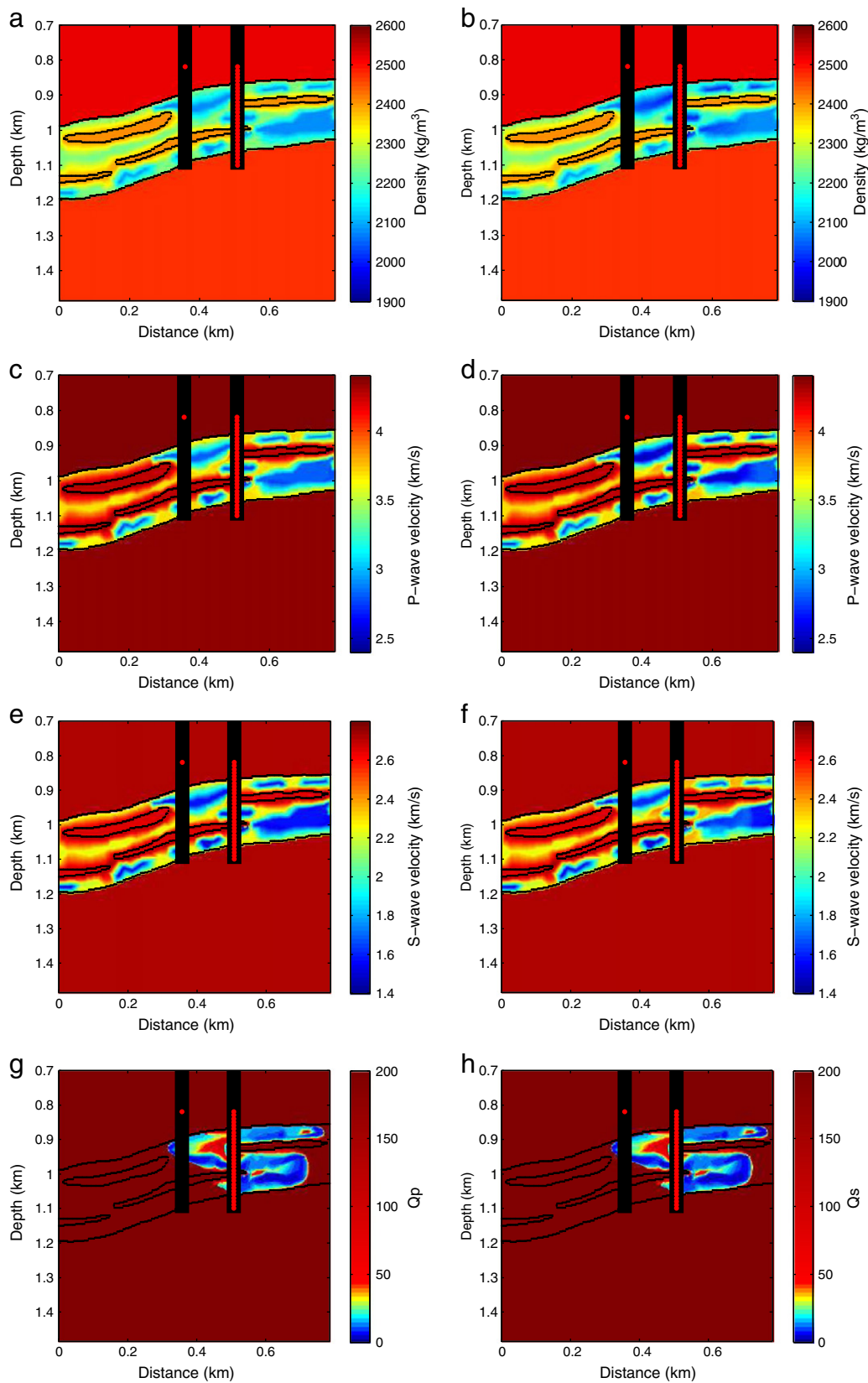
where  $T$  is the period of the wave and we take  $t_s = 1.4T$ . The peak frequency is  $f_p = 1/T$ . The simulations use an explosion as a source [ $f_{xx} = f_{zz}$  in Eqs. (25) and (26)] and a central frequency  $f_p = 150$  Hz. The time step of the Runge–Kutta algorithm is 0.1 ms.

Fig. 12 shows the electromagnetic simulation before and after the injection (black and red curves, respectively, in c and d). As can be seen, the traveltimes after the injection are lower due to the higher resistivity of the layer partially saturated with carbon dioxide. The seismic (viscoelastic) simulations are shown in Fig. 13 and in this case the traveltimes after the injection are higher than the traveltimes obtained for a water saturated aquifer.

In the upper part of the aquifer, the gas saturation after the injection is about 20–40% (see Fig. 9a). The conductivity has been reduced by a factor two, approximately from 1.6 S/m to 0.8 S/m (see Fig. 10), which generates a maximum traveltime difference (at receiver 15) of nearly 3 ms, before and after injection. This difference and the related conductivity contrast should be significant for a tomography inversion algorithm to detect the presence of gas (e.g., Lee and Uchida, 2005).



**Fig. 10.** Conductivity before (a) and after (b) CO<sub>2</sub> injection.



**Fig. 11.** Panels (a), (c), and (e) show the density, P-wave velocity and S-wave velocity before  $\text{CO}_2$  injection, respectively. Panels (b), (d) and (f) show the same properties after  $\text{CO}_2$  injection. Panels (g) and (h) show  $Q_p$  and  $Q_s$  at  $f_0$ , respectively, obtained from Eq. (4), after  $\text{CO}_2$  injection ( $Q_s = Q_0^{(2)}$ ).

In the seismic case, the differences in P-wave velocity range from 100 to 200 m/s (Fig. 11c and d) and P-wave quality-factor values are less than 50 (Fig. 11g). These differences in the

properties of the medium can safely be detected by means of traveltimes and attenuation tomography (Michellini, 1995; Rossi et al., 2007).

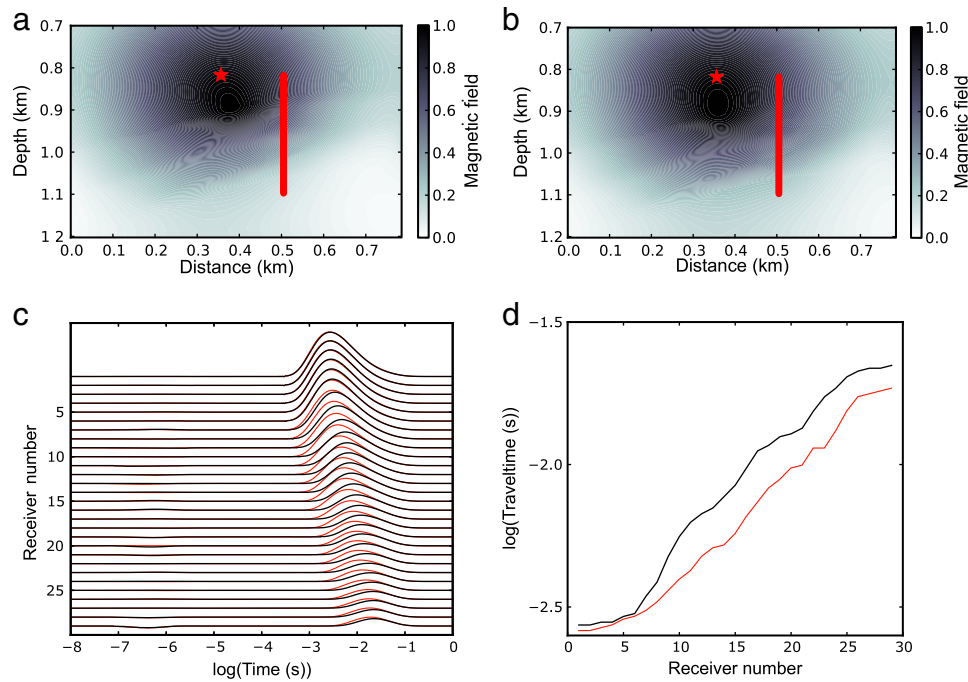


**Fig. 12.** Snapshots of the normalized magnetic field at 20 ms before (a) and after (b) CO<sub>2</sub> injection. The source and the vertical array of receivers are represented by the red star and vertical line, respectively. Panel (c) represents the normalized amplitude variation versus receiver number before and after injection (black and red curves, respectively), and panel (d) shows the traveltime picks before and after injection (dashed black and red curves, respectively). (For interpretation of the references to color in this figure caption, the reader is referred to the web version of this article.)

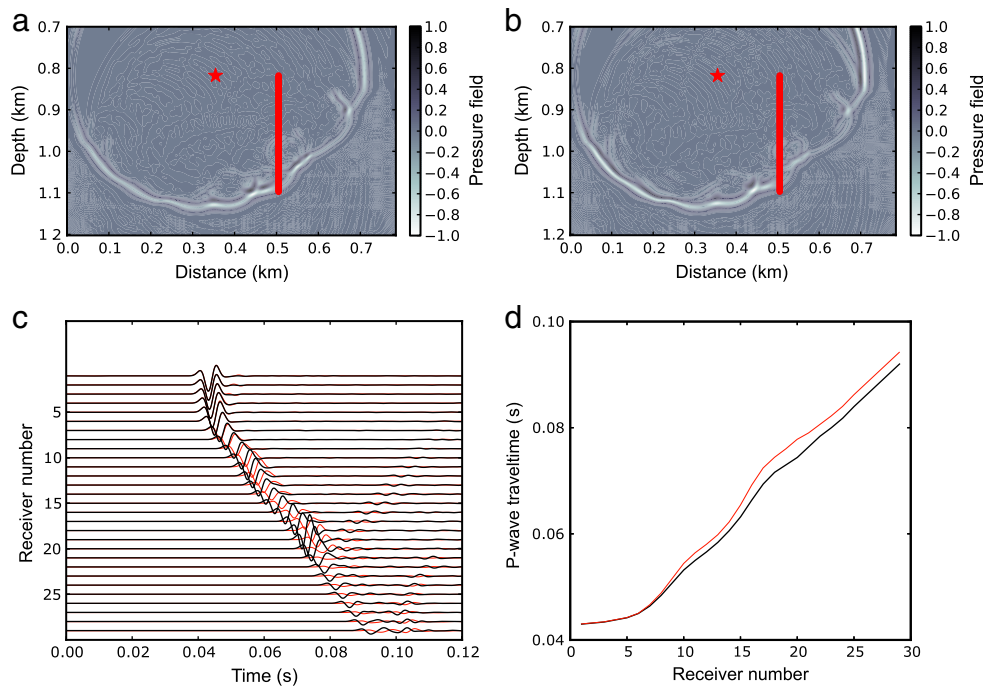


**Fig. 13.** Snapshot of the normalized pressure field at 90 ms before (a) and after the injection (b). The source and the vertical array of receivers are represented by the red star and vertical line, respectively. Panel (c) represents the normalized amplitude variation versus receiver number before and after injection (black and red curves, respectively), and panel (d) shows the traveltime picks before and after injection (dashed black and red curves, respectively). (For interpretation of the references to color in this figure caption, the reader is referred to the web version of this article.)

The combined use of traveltime and attenuation tomographies provides velocity-*Q*-factor sections (Rossi et al., 2007). Attenuation has been recognized as a significant seismic indicator, which is not only useful for amplitude analysis and improving resolution, but also to obtain information on lithology, saturation (fluid type), permeability and pore pressure (e.g., Carcione and Gangi, 2000).

## 5. Conclusions

Time-lapse surveys are essential to detect and monitor the presence of CO<sub>2</sub> in geological formations. The success of this process is subject to a correct description of the physical properties of the CO<sub>2</sub> bearing rocks and use of integrated geophysical



methods. We use the White/CRIM relation between seismic velocity and electrical conductivity, which has been successfully tested with well-log data. This integrated model constitutes a porous description of the geological formation, where grain properties, fluid types, porosity, clay content and permeability are explicitly considered, to obtain the electrical conductivity, seismic velocities and seismic quality factors.

Then, we compute the magnetic-field time histories and synthetic seismograms corresponding to a geological model of CO<sub>2</sub> partial saturation, based on a cross-hole source–receiver configuration, and obtain traveltimes picks (first arrival versus receiver locations), which are the basis for electromagnetic and seismic tomography. The computed fields before and after CO<sub>2</sub> injection show the expected differences, i.e., higher traveltimes in the electromagnetic case and lower traveltimes in the seismic case. Further research involves the use of various inversion techniques to obtain the location of the CO<sub>2</sub> bubble.

## Acknowledgment

This work was supported by projects CO2CARE and QUEST.

## Appendix A. White's mesoscopic model including S-wave dissipation

White (1975) assumed spherical patches much larger than the grains but much smaller than the wavelength. He developed the theory for a gas-filled sphere of porous medium of radius  $r_0$  located inside a water-filled sphere of porous medium of outer radius  $r_1$  ( $r_0 < r_1$ ). The saturation of gas is

$$S_g = \frac{r_0^3}{r_1^3} \quad \text{and} \quad S_b = 1 - S_g \quad (15)$$

is the brine saturation.

Assuming that the dry-rock and grain moduli and permeability,  $\kappa$ , of the different regions are the same, the complex bulk modulus as a function of frequency is given by

$$K = \frac{K_\infty}{1 - K_\infty W}, \quad (16)$$

where  $K_\infty$  is a – high frequency – bulk modulus when there is no fluid flow between the patches, and  $W$  is a compliance proportional to the permeability. The explicit expressions are not given here for brevity and can be found in Mavko et al. (1998), Carcione et al. (2003) and Picotti et al. (2010). For values of the gas saturation higher than 52%, or values of the water saturation between 0% and 48%, the theory is not rigorously valid. Another limitation to consider is that the size of gas pockets should be much smaller than the wavelength.

Clay content also affects the permeability. Carcione et al. (2000) derived a model of permeability as a function of clay content. They assumed that a shaly sandstone is composed of a sandy matrix and a shaly matrix with partial permeabilities

$$\kappa_q = \frac{R_q^2 \phi^3}{45(1-\phi)^2(1-C)} \quad \text{and} \quad \kappa_c = \frac{R_c^2 \phi^3}{45(1-\phi)^2 C}, \quad (17)$$

where  $R_q$  and  $R_c$  denote the average radii of sand and clay particles, respectively. Assuming that permeability is analogous to the inverse of the electrical resistance, the average permeability of the shaly sandstone is given by

$$\frac{1}{\kappa} = \frac{1-C}{\kappa_q} + \frac{C}{\kappa_c} = \frac{(1-\phi)^2}{A\phi^3} [(1-C)^2 + C^2 B^2], \quad (18)$$

where  $A = R_q^2/45$  and  $B = R_q/R_c$  or can be assumed as empirical parameters.

Since White's theory does not predict any shear dissipation, we assume that the complex modulus  $\mu$  is described by a Zener element having a peak frequency  $f_0$  and a minimum quality factor given by

$$Q_0^{(2)} = \frac{\mu_m}{\text{Re}[K(f_0)]} Q_0, \quad (19)$$

where  $Q_0$  is the quality factor associated with  $K$  at  $f_0$ , i.e.,

$$Q_0 = Q(f_0) = \frac{\text{Re}[K(f_0)]}{\text{Im}[K(f_0)]}. \quad (20)$$

The model for the anelastic dilatations is based on a poroelastic model, but the viscoelastic behavior of the shear waves is incorporated into the modeling in an ad hoc manner. The problem is the lack of a mesoscopic theory for shear deformations, i.e., something similar to White's model. To model the amount of loss related to the shear motions, we assume that the stiffer the medium the higher the quality factor (relation (19)), i.e., if the modulus increases the attenuation decreases and vice versa. However, the Zener model is consistent with White's theory, since both models describe anelasticity in the form of a relaxation peak in the frequency domain. Picotti et al. (2010) show that White's model can be represented by a Zener mechanical element.

Then, the dimensionless modulus is given by Eq. (31), and

$$\mu = \mu M_2, \quad (21)$$

where  $\mu$  and  $M_2$  are given in the next section. Note that  $Q_0$  depends on gas saturation. The frequency  $f_0$  is taken in the seismic frequency range in this work, particularly, equal to the source dominant frequency.

## Appendix B. Electromagnetic modeling

Eq. (12) has the form  $\partial_t H_y = \mathcal{O} H_y$ , with  $\mathcal{O} = [(\sigma^{-1} H_{y,x})_x + (\sigma^{-1} H_{y,z})_z]/\mu$ . The eigenvalue equation in the complex  $\lambda$ -domain ( $\lambda = -i\omega$ ), corresponding to operator  $\mathcal{O}$ , is  $\lambda[\lambda + D(k_x^2 + k_z^2)] = 0$ , where  $\omega$  is the frequency and  $D = 1/(\mu\sigma)$ . The eigenvalues are therefore zero and real and negative, and the maximum (Nyquist) wavenumber components are  $k_x = \pi/dx$  and  $k_z = \pi/dz$  for the grid spacings  $dx$  and  $dz$ . The solution of Eq. (12) can be obtained as

$$H_y(t) = \sum_{k=0}^M c_k \exp(-bt) I_k(tR) Q_k(\mathcal{O}/b + 1) H_{y0}, \quad (22)$$

where  $H_{y0}$  is a discrete spatial delta function applied at the source location,  $b$  is the absolute value of the largest eigenvalue of  $\mathcal{O}$ ,  $I_k$  is the modified Bessel function of order  $k$ ,  $c_0 = 1$  and  $c_k = 2$  for  $k \neq 0$ , and  $Q_k$  are modified Chebyshev polynomials. The value of  $b$  is equal to  $(\pi^2/D)(1/dx^2 + 1/dz^2)$ , while  $R$  should be chosen slightly larger than  $b$ . The maximum polynomial order  $M$  should be  $O(\sqrt{bt})$ . It can be shown that  $M = 6\sqrt{bt}$  is enough to obtain stability and accuracy (Carcione, 2006).

The algorithm is a three-level scheme, since it uses the recurrence relation of the Chebyshev polynomials. The solution is obtained at one large time step  $T$ . Results at smaller time levels,  $t < T$ , to compute time histories at specified points of the grid, do not require significant computational effort, since the terms involving the spatial derivatives do not depend on the time variable and are calculated in any case. Only the coefficients  $\exp(-bt) I_k(tR)$  are time dependent, such that additional sets of Bessel functions need to be computed. The intermediate time levels can be defined on a logarithm scale to better capture the peak of the first arrival (see Appendix D).

The boundaries of the mesh may produce wraparounds due to the periodic properties of the Fourier method. We use the classical damping approach to avoid these non-physical artifacts (Carcione, 2007; Kosloff and Kosloff, 1986). The method simply requires to modify the differential operator as  $\mathcal{O} \rightarrow \mathcal{O} - o$  in the absorbing strips around the mesh, where  $o$  is different from zero at narrow strips surrounding the mesh. Its value has to be optimized in such a way that the diffusion field agrees with an analytical solution at times much larger than the peak of the signal (see Appendix D).

### Appendix C. Viscoelastic differential equations

The time-domain equations for propagation in a heterogeneous viscoelastic medium can be found in Carcione (2007). The anelasticity is described by the standard linear solid, also called the Zener model, that gives relaxation and creep functions in agreement with experimental results.

The two-dimensional velocity–stress equations for anelastic propagation in the  $(x, z)$ -plane, assigning one relaxation mechanism to dilatational anelastic deformations ( $v = 1$ ) and one relaxation mechanism to shear anelastic deformations ( $v = 2$ ), can be expressed by

(i) Euler–Newton’s equations:

$$\dot{v}_x = \frac{1}{\rho}(\sigma_{xx,x} + \sigma_{xz,z}) + f_x, \quad (23)$$

$$\dot{v}_z = \frac{1}{\rho}(\sigma_{xz,x} + \sigma_{zz,z}) + f_z, \quad (24)$$

where  $v_x$  and  $v_z$  are the particle velocities,  $\sigma_{xx}$ ,  $\sigma_{zz}$  and  $\sigma_{xz}$  are the stress components,  $\rho$  is the density and  $f_x$  and  $f_z$  are the body forces.

(ii) Constitutive equations:

$$\dot{\sigma}_{xx} = k(v_{x,x} + v_{z,z} + e_1) + \mu(v_{x,x} - v_{z,z} + e_2) + f_{xx}, \quad (25)$$

$$\dot{\sigma}_{zz} = k(v_{x,x} + v_{z,z} + e_1) - \mu(v_{x,x} - v_{z,z} + e_2) + f_{zz}, \quad (26)$$

$$\dot{\sigma}_{xz} = \mu(v_{x,z} + v_{z,x} + e_3) + f_{xz}, \quad (27)$$

where  $e_1$ ,  $e_2$  and  $e_3$  are memory variables,  $f_{ij}$  are external sources, and  $k$  and  $\mu$  are the unrelaxed (high-frequency) bulk and shear moduli, respectively, given by in the next section.

(iii) Memory variable equations:

$$\dot{e}_1 = \left( \frac{1}{\tau_\epsilon^{(1)}} - \frac{1}{\tau_\sigma^{(1)}} \right) (v_{x,x} + v_{z,z}) - \frac{e_1}{\tau_\sigma^{(1)}}, \quad (28)$$

$$\dot{e}_2 = \left( \frac{1}{\tau_\epsilon^{(2)}} - \frac{1}{\tau_\sigma^{(2)}} \right) (v_{x,x} - v_{z,z}) - \frac{e_2}{\tau_\sigma^{(2)}}, \quad (29)$$

$$\dot{e}_3 = \left( \frac{1}{\tau_\epsilon^{(2)}} - \frac{1}{\tau_\sigma^{(2)}} \right) (v_{x,z} + v_{z,x}) - \frac{e_3}{\tau_\sigma^{(2)}}, \quad (30)$$

where  $\tau_\sigma^{(v)}$  and  $\tau_\epsilon^{(v)}$  are material relaxation times, corresponding to dilatational ( $v = 1$ ) and shear ( $v = 2$ ) deformations.

#### C.1. Propagation properties

The complex moduli associated with bulk and shear deformations are the Zener moduli,

$$M_v = \frac{\tau_\sigma^{(v)}}{\tau_\epsilon^{(v)}} \left( \frac{1 + i\omega\tau_\epsilon^{(v)}}{1 + i\omega\tau_\sigma^{(v)}} \right), \quad v = 1, 2, \quad (31)$$

where  $i = \sqrt{-1}$ , such that the relaxation times can be expressed as

$$\tau_\epsilon^{(v)} = \frac{\tau_0}{Q_0^{(v)}} (\sqrt{Q_0^{(v)} 2 + 1} + 1), \quad \tau_\sigma^{(v)} = \tau_\epsilon^{(v)} - \frac{2\tau_0}{Q_0^{(v)}}, \quad (32)$$

where  $\tau_0$  is a relaxation time such that  $1/\tau_0$  is the center frequency of the relaxation peak and  $Q_0^{(v)}$  are the minimum quality factors. The complex (viscoelastic) bulk and shear moduli are

$$\bar{K} = kM_1 \quad \text{and} \quad \mu = \mu M_2. \quad (33)$$

In order to obtain  $\mu$  and  $k$ , we express the P and S viscoelastic phase velocities as

$$c_P = \left[ \text{Re} \left( \frac{1}{v_P} \right) \right]^{-1} \quad \text{and} \quad c_S = \left[ \text{Re} \left( \frac{1}{v_S} \right) \right]^{-1}, \quad (34)$$

where

$$v_P = \sqrt{\frac{1}{\rho} \left( \bar{K} + \frac{4}{3}\mu \right)} \quad \text{and} \quad v_S = \sqrt{\frac{\mu}{\rho}}, \quad (35)$$

respectively. First, we obtain  $\mu$  as

$$\mu = \mu_m \left[ \text{Re} \sqrt{\frac{1}{M_2(f_0)}} \right]^2, \quad (36)$$

assuming  $\mu_m = \rho c_S^2(f_0)$ , and  $k$  is computed by solving

$$\text{Re} \sqrt{\frac{\rho}{kM_1(f_0) + 4\mu M_2(f_0)/3}} \frac{1}{c_P(f_0)} = 0. \quad (37)$$

### Appendix D. Electromagnetic Green’s function and traveltimes picking

Traveltimes tomography is based on the first arrival at each receiver (e.g., Michelini, 1995). To illustrate the physics we consider a solution of Eq. (12) in the case of isotropic homogeneous media. The Green function corresponding to Eq. (38), with  $J_x = J_z = 0$ , and a magnetic source

$$M_y(x, y, t) = M_0 \delta(x) \delta(z) [1 - H(t)], \quad (38)$$

is the solution of

$$\partial_t H_y = D \Delta H_y + M_0 \delta(x) \delta(z) \delta(t), \quad (39)$$

where  $M_0$  defines the direction and the strength of the source, and

$$D = \frac{1}{\mu\sigma} \quad (40)$$

is the diffusivity. Eq. (39) has the following solution (Green’s function):

$$H_y(r, t) = \frac{M_0}{(4\pi Dt)^{N/2}} \exp[-r^2/(4Dt)], \quad (41)$$

where  $N$  is the space dimension ( $N=2$  in this work), and

$$r = \sqrt{x^2 + z^2} \quad (42)$$

(Carcione, 2010; Carslaw and Jaeger, 1959; Oristaglio and Hohmann, 1984).

The solution  $H_y(t)$  has a maximum at

$$t_p = \frac{r^2}{4D} = \frac{\mu\sigma r^2}{4} \quad (43)$$

[ $t_p = r^2/(6D)$  in 3D space]. Then, in a homogeneous medium, the conductivity can simply be obtained as  $\sigma = 4t_p/(\mu r^2)$ , at a source–receiver distance  $r$ . Eq. (43) indicates that the diffusion is faster in resistive media. The phase velocity and attenuation factor for

planes waves is

$$\nu_p = 2\sqrt{\frac{\pi f}{\mu\sigma}}, \quad \text{and} \quad \alpha = \sqrt{\pi f \mu\sigma}, \quad (44)$$

respectively, where  $f$  is the frequency (e.g., Carcione, 2007);  $\alpha$  is the reciprocal of the skin depth and therefore the penetration is less in more conductive media.

In inhomogeneous media we need to perform traveltime tomography (e.g., Brauchler et al., 2003), which is based on the following line integral:

$$\sqrt{t_p} = \frac{1}{4} \int_{x_1}^{x_2} \frac{ds}{\sqrt{D}}, \quad (45)$$

where  $x_1$  and  $x_2$  refer to the source and receiver locations, respectively. The procedure is similar to seismic traveltime tomography, where the line integral has the form  $t_p = \int ds/\nu_p$ , with  $\nu_p$  the wave velocity (Michellini, 1995). In our case, one has to find the diffusivity (or conductivity) model that minimizes the functional  $\sum_i^n (\sqrt{t_i^m} - \sqrt{t_i})^2$ , where  $t_i^m$  is the measured traveltime and  $t_i$  is the ray-tracing (computed) traveltime. The first break is obtained as the time that the first derivative of the field is maximum (Yu and Edwards, 1997). An alternative picking method is given in Lee and Uchida (2005).

## References

- Alavian, S.A., Whitson, C.H., 2011. Numerical modeling CO<sub>2</sub> injection in a fractured chalk experiment. *J. Pet. Sci. Eng.* 77, 172–182.
- Arts, R., Eiken, O., Chadwick, R.A., Zweigel, P., Van der Meer, L., Zinszner, B., 2004. Monitoring of CO<sub>2</sub> injected at Sleipner using time-lapse seismic data. *Energy* 29, 1383–1392.
- Bourgeois, B., Rohmer, J., Girard, J.-F., 2009. Numerical modelling of the time-lapse EM response of a CO<sub>2</sub> injection in a deep saline aquifer using metallic casings for the current injection. In: AAPG/SEG/SPE Hedberg Conference, "Geological Carbon Sequestration: Prediction and Verification", Vancouver, Canada.
- Brauchler, R., Liedl, R., Dietrich, P., 2003. A travel time based hydraulic tomographical approach. *Water Resour. Res.* 39, 1370, <http://dx.doi.org/10.1029/2003WR002262>.
- Carcione, J.M., 2006. A spectral numerical method for electromagnetic diffusion. *Geophysics* 71, 11–19.
- Carcione, J.M., 2007. Wave Fields in Real Media. Theory and Numerical Simulation of Wave Propagation in Anisotropic, Anelastic, Porous and Electromagnetic Media, second ed. Elsevier.
- Carcione, J.M., 2010. Simulation of electromagnetic diffusion in anisotropic media. *Prog. Electromagnetics Res. B (PIER B)* 26, 425–450.
- Carcione, J.M., Gangi, A., 2000. Non-equilibrium compaction and abnormal pore-fluid pressures: effects on seismic attributes. *Geophys. Prospect.* 48, 521–537.
- Carcione, J.M., Gurevich, B., Cavallini, F., 2000. A generalized Biot–Gassmann model for the acoustic properties of shaley sandstones. *Geophys. Prospect.* 48, 539–557.
- Carcione, J.M., Helle, H.B., Pham, N.H., 2003. White's model for wave propagation in partially saturated rocks: comparison with poroelastic numerical experiments. *Geophysics* 68, 1389–1398.
- Carcione, J.M., Kosloff, D., Kosloff, R., 1988. Wave propagation simulation in a linear viscoelastic medium. *Geophys. J. R. Astron. Soc.* 95, 597–611.
- Carcione, J.M., Picotti, S., Gei, D., Rossi, G., 2006. Physics and seismic modeling for monitoring CO<sub>2</sub> storage. *Pure Appl. Geophys.* 163, 175–207.
- Carcione, J.M., Ursin, B., Nordskag, J.L., 2007. Cross-property relations between electrical conductivity and the seismic velocity of rocks. *Geophysics* 72, E193–E204.
- Carslaw, H.S., Jaeger, J.C., 1959. *Conduction of Heat in Solids*. Clarendon Press.
- Christensen, N.B., Sherlock, D., Dodds, K., 2006. Monitoring CO<sub>2</sub> injection with cross-hole electrical resistivity tomography. *Explor. Geophys.* 37, 44–49.
- David, E.C., Zimmerman, R.W., 2011. Elastic moduli of solids containing spheroidal pores. *Int. J. Eng. Sci.* 49, 544–560.
- Giese, R., Henningses, J., Lüth, S., Morozova, D., Schmidt-Hattenberger, C., Würdemann, H., Zimmer, M., Cosma, C., Juhlin, C., 2009. CO<sub>2</sub> SINK Group, 2009. Monitoring at the CO<sub>2</sub> SINK site: a concept integrating geophysics, geochemistry and microbiology. *Energy Procedia* 1, 2251–2259.
- Hagrey, S.A., 2010. CO<sub>2</sub> plume modeling in deep saline reservoirs by 2D ERT in boreholes. *The Leading Edge* 30, 24–33.
- Hashin, Z., Shtrikman, S., 1963. A variational approach to the theory of the elastic behaviour of multiphase materials. *J. Mech. Phys. Solids* 11, 127–140.
- Hoversten, G.M., Cassacuce, F., Gasperikova, E., Newman, G.A., Chen, J., Rubin, Y., Hou, Z., Vasco, D., 2006. Direct reservoir parameter estimation using joint inversion of marine seismic AVA and CSEM data. *Geophysics* 71, C1–C13.
- Hoversten, G.M., Milligan, P., Byun, J., Washbourne, J., Knauerzz, L.C., Harnesszz, P., 2004. Crosswell electromagnetic and seismic imaging: an examination of coincident surveys at a steam flood project. *Geophysics* 69, 406–414.
- Kachanov, M., Sevostianov, I., Shafiro, B., 2001. Explicit cross-property correlations for porous materials with anisotropic microstructures. *J. Mech. Phys. Solids* 49, 1–25.
- Kosloff, D., Kosloff, R., 1986. Absorbing boundaries for wave propagation problems. *J. Comput. Phys.* 63, 363–376.
- Lee, T.J., Suh, J.H., Kim, H.J., Song, Y., Lee, K.H., 2002. Electromagnetic traveltime tomography using an approximate wavefield transform. *Geophysics* 67, 68–76.
- Lee, T.J., Uchida, T., 2005. Electromagnetic traveltime tomography: application for reservoir characterization in the Lost Hills oil field, California. *Geophysics* 70, G51–G58.
- Lei, X., Xue, Z., 2009. Ultrasonic velocity and attenuation during CO<sub>2</sub> injection into water-saturated porous sandstone: measurements using difference seismic tomography. *Phys. Earth Planet. Inter.* 176, 224–234.
- Le Ravalec, M., Gueguen, Y., 1996. High- and low-frequency elastic moduli for a saturated porous/cracked rock-differential self-consistent and poroelastic theories. *Geophysics* 61, 1080–1094.
- Li, H., Zhang, J., 2011. Analytical approximations of bulk and shear moduli for dry rock based on the differential effective medium theory. *Geophys. Prospect.*, <http://dx.doi.org/10.1111/j.1365-2478.2011.00980.x>.
- Mavko, G., Mukerji, T., Dvorkin, J., 1998. *The Rock Physics Handbook: Tools for Seismic Analysis in Porous Media*. Cambridge University Press.
- Michellini, A., 1995. An adaptive-grid formalism for traveltime tomography. *Geophys. J. Int.* 121, 489–510.
- Norman, T., Alnes, H., Christensen, O., Zach, J.J., Eiken, O., Tjaland, E., 2008. Planning time-lapse CSEM-surveys for joint seismic-EM monitoring of geological carbon dioxide injection. In: EAGE CO<sub>2</sub> Geological Storage Workshop, Budapest, Hungary.
- Oristaglio, M.L., Hohmann, G.W., 1984. Diffusion of electromagnetic fields into a two-dimensional earth: a finite-difference approach. *Geophysics* 49, 870–894.
- Picotti, S., Carcione, J.M., Rubino, G., Santos, J.E., Cavallini, F., 2010. A viscoelastic representation of wave attenuation in porous media. *Comput. Geosci.* 36, 44–53.
- Rossi, G., Gei, D., Böhm, G., Madrussani, G., Carcione, J.M., 2007. Attenuation tomography: an application to gas-hydrate and free-gas detection. *Geophys. Prospect.* 55, 655–669.
- Schön, J.H., 1996. *Physical Properties of Rocks. Handbook of Geophysical Exploration*. Pergamon Press.
- White, J.E., 1975. Computed seismic speeds and attenuation in rocks with partial gas saturation. *Geophysics* 40, 224–232.
- Wilt, M.J., Alumbaugh, D.L., Morrison, H.F., Becker, A., Lee, K.H., Deszcz-Pan, M., 1995. Crosswell electromagnetic tomography—system design considerations and field results. *Geophysics* 60, 871–885.
- Yu, L., Edwards, R.N., 1997. On crosswell diffusive time-domain electromagnetic tomography. *Geophys. J. Int.* 130, 449–459.